Highly transparent Ce3+,Cr3+ co-doped GYAGG single crystals with enhanced persistent luminescence

Teresa Delgado, Daniel Rytz, Guanyu Cai, Mathieu Allix, Emmanuel Veron, Ida Di Carlo, Bruno Viana

To cite this version:

Teresa Delgado, Daniel Rytz, Guanyu Cai, Mathieu Allix, Emmanuel Veron, et al.. Highly transparent Ce3+,Cr3+ co-doped GYAGG single crystals with enhanced persistent luminescence. Ceramics International, 2023, 10.1016/j.ceramint.2023.02.249 . insu-04043838

Ceramics International xxx (xxxx) xxx

Contents lists available at ScienceDirect

Ceramics International

journal homepage: www.elsevier.com/locate/ceramint

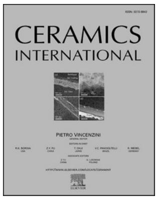

Highly transparent Ce^{3+},Cr^{3+} co-doped GYAGG single crystals with enhanced persistent luminescence

Teresa Delgado [a,*], Daniel Rytz [b], Guanyu Cai [a], Mathieu Allix [c], Emmanuel Veron [c], Ida di Carlo [d], Bruno Viana [a,**]

[a] *PSL University, Chimie ParisTech, IRCP-CNRS, Paris, 7505, France*
[b] *BREVALOR Sàrl, 1669, Les Sciernes, Switzerland*
[c] *CNRS, CEMHTI UPR 3079, Univ. Orléans, 45071, Orléans, France*
[d] *Univ. Orléans, CNRS, BRGM, ISTO, UMR 7327, F-45071, Orléans, France*

ARTICLE INFO

Handling Editor: Dr P. Vincenzini

Keywords:
Persistent luminescence
Storage materials
Garnet crystals

ABSTRACT

Despite significant interest in persistent luminescence materials, the focus of all recent works remains on the exploitation of materials in powder form. Here, a new point of view based on persistent luminescence in single crystals is presented. The garnet crystals $[(Gd_{0.67}Y_{0.33})_{3\text{-}x}Ce_x)](Al_{2\text{-}y}Cr_y)Ga_3O_{12}$ and $[(Gd_{0.33}Y_{0.67})_{3\text{-}x}Ce_x](Al_{2\text{-}y}Cr_y)Ga_3O_{12}$ (GYAGG) codoped with Ce^{3+} and different concentrations of Cr^{3+} have been elaborated and their persistent luminescence properties are fully characterized within this work. The persistent luminescence of Ce^{3+}, Cr^{3+}-codoped GYAGG single crystals is optimized due to their high optical quality, very good crystallinity and a volume effect where the whole material can be excited and charged by the excitation light. Furthermore, thanks to their transparency, robustness and homogeneity; in-depth optical spectroscopy characterization is possible, shedding light on the mechanism responsible for the afterglow.

1. Introduction

Studies about persistent luminescence or afterglow materials are increasingly popular. A quick search on published articles and patents on Google scholar of these two terms in 2022 shows 12,000 entries. This is due to their very broad range of applications that extend from core uses as indoor lighting [1], sensing [2,3], watch components [4], textiles [5,6], dosimetry [7], anti-counterfeiting [8,9], bioimaging [10–12] and therapy [13–16] to emerging applications combating the greenhouse effect such as road marking and lighting of outdoor cycling paths [17], stimulation of photosynthesis and regulation of photomorphogenesis in plants [18], feeding of solar cells [19–21] or even applications related to human wellbeing such as facilitating sleep. The persistent luminescence in solid-state inorganic phosphors is related to the trapping of charge carriers in defect electronic states and their delayed release upon time or temperature [1,22,23]. The origin of these defects can be related to vacancies, colour centres or the introduction of different dopants with equal (or slightly different) charge and size in regards to the cations forming the host [22,23].

In this sense, Ce^{3+} and Cr^{3+} co-doped gadolinium-yttrium-aluminium-gallium garnets of general formula $Y_{3\text{-}x}Gd_xAl_2Ga_3O_{12}$ (GYAGG), whose structure can be found elsewhere [24], are defined as afterglow materials where the Ce^{3+} acts as an active center and the Cr^{3+} as electron trap. The former, which is responsible for the yellow persistent luminescence due to the 5d-4f emission, sits in the dodecahedral site of Y^{3+} and the Cr^{3+} cations, that act as electron trapping centres, are located in the octahedral sites of Al^{3+} or Ga^{3+}. In addition, the band gap of the original host $Y_3Al_5O_{12}$ (YAG) is diminished by the insertion of Ga^{3+} ions that sit in the (either octahedral or tetrahedral) Al^{3+} sites and an optimum performance is typically obtained for a (Al_2Ga_3) composition instead of (Al_5) [25]. On the other hand, Gd^{3+}, which is introduced to facilitate the insertion of Ce^{3+}, is located in the dodecahedral site of Y^{3+}. Therefore, by modification of the cationic composition, the band gap is modified to optimize the persistent luminescence as well as to tune the excited energy levels of Ce^{3+}. Broadly speaking, the introduction of Gd^{3+} and Ga^{3+} in these materials leads to a decrease of the band gap of the host and to a better control of the kinetics [26,27].

---

[*] Corresponding author.
[**] Corresponding author.
E-mail address: teresa.delgado@chimieparistech.psl.eu (T. Delgado).

https://doi.org/10.1016/j.ceramint.2023.02.249
Received 27 December 2022; Received in revised form 26 February 2023; Accepted 28 February 2023
Available online 2 March 2023

Please cite this article as: Teresa Delgado et al., *Ceramics International*, https://doi.org/10.1016/j.ceramint.2023.02.249

It is important to indicate that in the absence of chromium, Ce^{3+}-doped $Y_3Al_2Ga_3O_{12}$ (YAGG) presents yellow afterglow due to defect traps (oxygen vacancies, antisite defects, etc. That can be controlled by bandgap engineering etc.) [28–30]. These traps are relatively shallow (close to the conduction band), thus the duration of the persistent luminescence is shorter than in Ce^{3+}, Cr^{3+}-codoped YAGG and are mostly used for white LED light converters [31]. It is interesting to point out that the yellow luminescence of Ce^{3+} in YAGG has been tuned towards red upon incorporation of super-high amount of this ion [32]. This red shift is related to a softening of the crystal lattice upon higher concentrations of the cations due to a tetragonal distortion of the CeO_8 moieties in the material that leads to a larger crystal-field splitting [33]. In the same line, in the absence of cerium, Cr^{3+}-doped YAGG presents red afterglow after UV or even NIR excitation for more than 1 h with quite high irradiance compared to other red persistent phosphors such as $ZnGa_2O_4:Cr^{3+}$ [34]. In that case, it has been defended that the Cr^{3+} ions can act as both hole and electron traps forming Cr^{4+} and Cr^{2+}, respectively [35].

Likewise, other co-dopants different than Cr^{3+} can be used in Ce^{3+}-doped YAGGs samples [36]. This is the case for instance of Ce^{3+}, Sr^{2+}-doped [37] and Ce^{3+},V^{3+}-doped [38] YAGG with improved luminescent properties. In particular, Ce^{3+}, Yb^{3+} -doped YAGG shows an extraordinary long persistent luminescent time due to the creation of very deep traps [39]. With a third dopant such as B^{3+}, which is in principle added as a flux, Ce^{3+}, Yb^{3+}, B^{3+}-doped YAGG exhibits very deeps traps (~1.10 eV) [40] as in the well-known $SrAl_2O_4:Eu^{2+}$,Dy^{3+}, B^{3+} persistent luminescence material [41–43]. In the same line, other activators as Pr^{3+} or Tb^{3+} instead of Ce^{3+} with ground states above the valence band (VB) [44] have been used in YAGG together with Cr^{3+} to tune the persistent luminescence towards orange and green light emission, respectively. Other combinations like Dy^{3+}-Cr^{3+} and Nd^{3+}-Cr^{3+} were also tried with much weaker red luminescence only due to Cr^{3+} [45]. YAGG:Cr^{3+} samples have been codoped with Er^{3+} for NIR I/III emission upon red excitation thanks to traps redistribution and persistent energy transfer [46]. In a further step, YAGG: Ce^{3+}, Cr^{3+} phosphors codoped either with Nd^{3+} or with Er^{3+} for persistent luminescence emission upon blue excitation in the NIR-I/NIR-II [47] and NIR-III [48], respectively, have been elaborated. This is of crucial importance since persistent luminescence in the NIR-II, III and IV biological windows would strongly reduce the problem of the autofluorescence of body tissues [49,50]. In the case of Nd^{3+} doping, downsizing to the nanoscale, which is essential for bioimaging, has been achieved by a microemulsion method [51] and solvothermal reaction [52]. In the same line, persistent luminescence nanoparticles (PLNPs) of YAGG: Ce^{3+}, Cr^{3+}, Pr^{3+} with average size of 50 nm have been recently obtained by co-precipitation [53]. Finally, the use of Gd^{3+} instead of Y^{3+} (GAGG) led to 100 nm paramagnetic GAGG: Ce^{3+}, Cr^{3+} PLNPs useful for multifunctional (optical and magnetic) bioimaging [54]. Other applications of garnets in persistent luminescence include the use of $Y_3Al_2Ga_3O_{12}:Pr^{3+}$ as ultraviolet (UV) persistent phosphor [55], with the advantage that UV persistent luminescence has no spectral overlap with indoor ambient light.

Furthermore, Ce^{3+}, Cr^{3+}-doped GAGG [56] and YAGG [57] transparent ceramics show improved persistent luminescence in regards to the corresponding pellets or non-compacted powders thanks to volume effect. Recently transparent persistent luminescent films of these materials with dynamic chromaticity have been elaborated [58].

Here we present for the first time a study of Ce^{3+}, Cr^{3+}-doped GYAGG single crystals with very high optical quality. The goal is threefold: first, from a fundamental point of view we intend to shed light into the mechanism of the persistent luminescence taking advantage of the lack of surface defects in comparison with powder samples. Defects are beneficial or detrimental depending on the trap depth they give rise to, so we cannot make, a priory, a general statement on whether the lack of surface defects enhances the performance. However, the crystallinity of the sample and the volume effect enhance the performance as we can excite the whole material including the inner part due to the lower scattering in respect to the powder. Second, these studies will lead to afterglow intensity and duration improvements as precise control of the composition is possible by absorption spectroscopy thanks to the high transparency of the crystals. Indeed, not only the dopants amount is optimized but also the Y/Gd ratio to shift the excitation spectra towards longer wavelengths, that is, to improve the efficiency of these materials at sun light excitation. Besides, crystals offer the possibility of measuring trapping defects by absorption spectroscopy thanks to the longer optical path. Third, surface optimization leading to better performance and tuning of the afterglow wavelengths is also demonstrated within this study in these crystals.

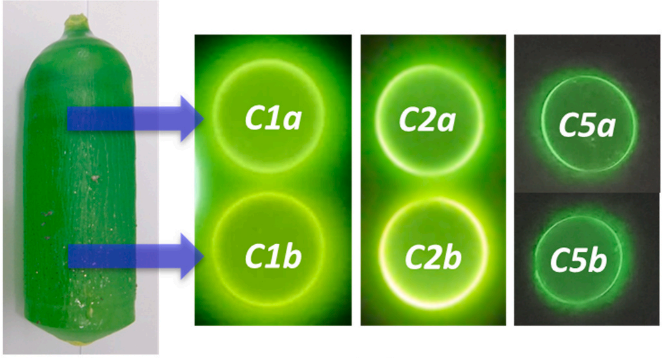

Fig. 1. Image of a typical Czochralski boule of Ce^{3+},Cr^{3+}: GYAGG (left) and (right) images of the polished section disks (crystals under study) from the upper (named a) and lower part (named b). The crystal's diameter is 9.3 mm and the thickness 1.5 mm. In the right side the crystals are being excited by UV light.

2. Experimental section

2.1. Crystal elaboration

The garnet single crystals used in the present study were obtained by a procedure developed by BREVALOR and were grown by pulling from the melt using a Czochralski-type process (Fig. 1). The resulting crystal samples are highly transparent (Fig. S2), i.e., their optical transmission (in wavelength ranges where no absorption is expected) is close to the value expected after correction for internal reflection losses. In total, 5 main crystals compositions are presented in this work, hereafter named as CX. The nominal composition for the first three GYAGG crystals (C1.1, C1.2, C1.3) can be written as $[(Gd_{0.67}Y_{0.33})_{3\text{-}x}Ce_x)](Al_{2\text{-}y}Cr_y)Ga_3O_{12}$ with almost the same Ce^{3+} content and different concentrations of Cr^{3+} (see absorption and microprobe analysis hereafter.) The nominal composition for the GYAGG crystal C5 is $[(Gd_{0.33}Y_{0.67})_{3\text{-}x}Ce_x](Al_{2\text{-}y}Cr_y)$ Ga_3O_{12} This implies that the crystals C1.1-C1.3 contain a Gd/Y ratio of 2/3 whereas for crystal C5 the Gd/Y ratio is 1/3. Typically, the Cr concentration is around 0.1% [58]. For each nominal composition, two different samples are selected from the original crystal (Fig. 1), one from the upper part (CXa) and one from the bottom part (CXb) in order to take into account the segregation coefficients of Cr (expected to be > 1) and Ce (expected to be around 0.1 to 0.4). Due to dopant segregation, Cr^{3+} content is expected larger for all crystals in the upper position (in CXa in regards to CXb) while Ce^{3+} content is expected to be higher in CXb. Notice in Fig. 1 the slightly different persistent luminescence color from yellow to green when going from C1.1-3 to C5. From the grown Czochralski boules (average diameter and length 3.5 and 6 cm, respectively), disks of the crystals are cut and processed (with fine ground or polished surfaces) in order to define geometries and volumes, states of surfaces or structuration.

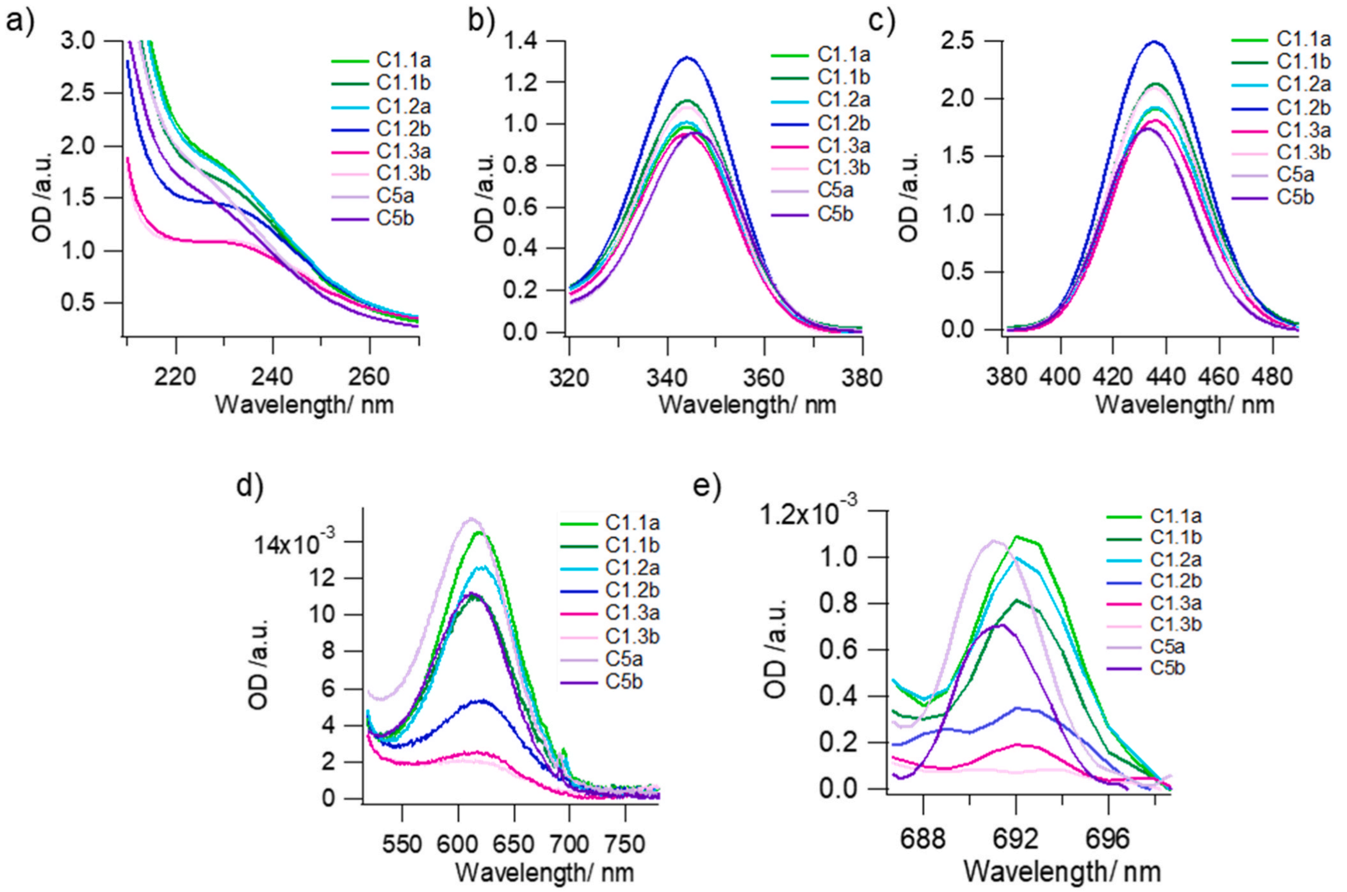

f)

C1.1a: $(Gd_{0.60}Y_{0.4})_{3.08(4)}\,Ce_{0.007(1)}\,(Al_{2.27(2)}\,Ga_{2.64(3)}\,Cr_{X})\,O_{12}$

C1.1b: $(Gd_{0.61}Y_{0.39})_{3.02(4)}\,Ce_{0.008(1)}\,(Al_{2.30(3)}\,Ga_{2.67(3)}\,Cr_{X})\,O_{12}$

C1.2a: $(Gd_{0.62}Y_{0.38})_{3.03(3)}\,Ce_{0.007(1)}\,(Al_{2.24(1)}\,Ga_{2.72(2)}\,Cr_{X})\,O_{12}$

C1.2b: $(Gd_{0.64}Y_{0.36})_{3.03(3)}\,Ce_{0.008(1)}\,(Al_{2.17(2)}\,Ga_{2.78(3)}\,Cr_{X})\,O_{12}$

C1.3a: $(Gd_{0.64}Y_{0.36})_{3.03(4)}\,Ce_{0.007(1)}\,(Al_{2.19(2)}\,Ga_{2.77(2)}\,Cr_{X})\,O_{12}$

C1.3b: $(Gd_{0.65}Y_{0.35})_{3.03(4)}\,Ce_{0.008(1)}\,(Al_{2.17(2)}\,Ga_{2.79(2)}\,Cr_{X})\,O_{12}$

C5a: $(Gd_{0.26}Y_{0.74})_{3.09(2)}\,Ce_{0.008(1)}\,(Al_{2.36}Ga_{2.54}Cr_{X})\,O_{12}$

C5b: $(Gd_{0.26}Y_{0.74})_{3.08(2)}\,Ce_{0.007(4)}\,(Al_{2.36}Ga_{2.55}Cr_{X})\,O_{12}$

Fig. 2. Absorption (optical density) spectrum of the crystals (same thickness of 0.6 mm for all samples) collecting the above described $^4f_0$-$^5d_1$ transitions of Ce^{3+} (a–c) and d-d transitions of Cr^{3+} (d–e) $^4T_2 \rightarrow {}^4A_2$ and $^2E \rightarrow {}^4A_2$ for (d) and (e) respectively. f) Microprobe analysis results. Notice that x values of Cr^{3+} contents could not be determined within these measurements.

2.2. Absorption spectroscopy

Absorption measurements were carried out in a UV/Vis/NIR spectrophotometer (Varian-Agilent Cary 6000) from 200 to 800 nm. The resolution for the broad Ce^{3+} bands is 1 nm while being 0.1 nm for the Gd^{3+} and Cr^{3+} bands.

2.3. Thermoluminescence

Thermoluminescence (TL) measurements were performed using a closed-cycle He-flow cryostat (Sumitomo Cryogenics HC-4E) attached with a Lakeshore 340 temperature controller. The samples were cooled down to 10 K and irradiated with different LEDs (Thorlabs) during 10 min, except in the case of sunlight excitation where the samples were excited at room temperature (RT) with a Solar simulator (Abet technologies, Sun2000) for 10 min as well. Then the TL curves were recorded at a 10 K/min ramp while heating up to 470 K. The signal was recorded by a CCD camera (Roper Pixis 100) coupled to a visible monochromator (Acton Spectra Pro, Princeton Instruments, 300 grooves per mm, centred at 500 nm).

2.4. *Persistent luminescence*

The samples were loaded with a 455 nm LED (Thorlabs) during 10 min at 290 K and the persistent luminescence was detected from 1 min after cutting the excitation during 1 h at the same temperature. The signal was followed with the same CCD camera as in the TL experiment. Afterglow curves were obtained by integrating the intensity of the persistent luminescence spectra as a function of time.

2.5. *Quantum yield*

The quantum yield of fluorescence (QY_{fluor}) measurements were performed in an Integrating Sphere coupled with an AVANTES spectrometer. The data was analyzed with the AVASOFT software. Before the measurement, each sample was previously heated to 200 °C in a heating plate for thermal detrapping. All values were corrected from re-absorption by placing at first the crystals aside in the integrating sphere (not aligned with the LED). If the re-absorption is not considered, the final QY_{fluor} value is overestimated by 1%. For more details about the calculation of the QY_{fluor} value see Ref. [59].

2.6. *Microprobe analysis*

Prior to analyses, samples were carbon coated (15–20 nm) under vacuum. Analyses of crystals were performed with a Cameca SX Five electron microprobe (EMP) of the joint BRGM–CNRS facility at Orleans. Analyses were carried out under an acceleration voltage of 15 kV, a sample current of 10 nA and a counting time of 10 s for all elements on each spot (except for Ce: 100 s). For all samples a focused beam of 1 μm was used.

3. Results

3.1. *Absorption spectroscopy*

First, the influence of the persistent luminescence in the absorption spectrum of the crystals was evaluated. We have previously observed for other persistent luminescence materials such as $SrAl_2O_4:Eu^{2+},Dy^{3+}$ an artefact leading to lower absorption values since the detector cannot discern between the not-absorbed transmitted light and the luminescence of the sample [59]. In Fig. S1a it is shown that the absorption spectrum of C1.2a does not change during the afterglow or loading of the crystal hence the persistent luminescence will not play a role in absorption spectra.

The second thing to mention is the high transparency of the GYAGG crystals, which is reflected into the close to zero absorption of the spectra of all the crystals at 800 nm indicating a very high crystal quality with low residual absorption and low scattering centres density (Fig. S2a). Considering Ce^{3+}, two main absorption bands are observed in the GYAGG crystals at 436 and 344 nm, associated with the two first-excited level 5 d^1 (Fig. 2c) and 5 d^2 (Fig. 2b), respectively. These bands appear at 427 and 348 nm, respectively in YAGG (Figs. S1c and b, respectively). Indeed, upon Gd^{3+} addition in GYAGG, the crystal field around Ce^{3+} is stronger and the 5 d^1 stabilizes whereas the 5 d^2 destabilizes, hence the corresponding bands in the GYAGG crystals are shifted to lower and higher energies in the spectra, respectively favouring their excitation by blue light at 450 nm. According to previous literature, the three other 5 $d^{3\text{-}5}$ bands should appear at about 263, 227 and 207 nm respectively [26]. The first one was proved to be defect-related since it is present in undoped YAG. This band does not appear in the GYAGG crystals, probably due to a lower amount of defects. We observe however the 227 nm band thanks to the high transparency of the crystals (Fig. 2a). Concerning the bands associated with Cr^{3+}, two are observed at 616 (Fig. 2d) and 693 nm (Fig. 2f) corresponding to the $^4A_2$- $^4T_2$ and $^4A_2$- ^2E transitions, respectively, the second one being much less intense as it is spin forbidden (see the corresponding 3 d^3-Tanabe–Sugano diagram in octahedral crystal field in Ref. [60]).

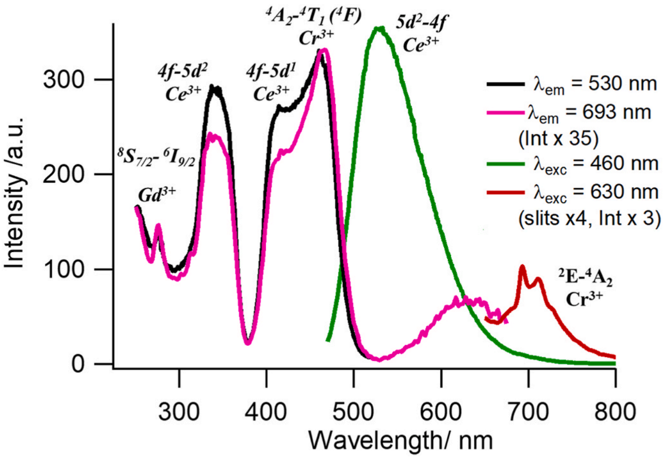

Fig. 3. Excitation and fluorescence spectra of $(Gd_{0.61}Y_{0.39})_{3.02(4)}$ $Ce_{0.008(1)}$ $(Al_{2.30(3)}$ $Ga_{2.67(3)}$ $Cr_X)$ O_{12}.

Most important, the comparison of crystals with different amounts of Ce^{3+} and Cr^{3+} allows us to determine the relative concentration of both cations within the host and calculate the extinction α coefficient, (Table S1), which is useful afterwards to estimate the concentrations of any kind of sample, crystal or powder by knowing their thickness and absorption spectrum [59] The first thing to notice is that the upper part of the crystals (CXa) always contain more Cr and less Ce than the lower part (CXb) due to the higher segregation coefficient of the Cr ions. The second is that the amount of Ce is almost the same in C1.1 and C1.2 crystals and slightly lower in C1.3 and higher in C5. Regarding the amount of Cr, it is again almost the same for C1.1 and C1.2, and slightly superior in C5 but significantly lower in C1.3 (between 7 and 10 times lower) as for the C1.1, C1.2 and C1.3 crystals elaboration, the same melt was used without adding chromium in the crucible. It is worth mentioning that whether we calculate α_{Ce3+} or α_{Cr3+} based on the bands of Fig. 1b and c or 1d,e, respectively, we obtain almost the same results and the same trend occurs for the two series of crystals, one with significantly thicker crystals of the same compositions (1.5 mm and 0.6 mm thick crystals) (Fig. S3, Table S1 where the absorption coefficients are given in two part of the single crystals at the beginning of the crystals growth and at the end, in the top and button of the Czochralski boule respectively. Notice in Fig. S3 that the absorption strengths for Ce^{3+} and Cr^{3+} are very different related to the parity allowed and forbidden transition respectively. Thicker crystals show as well an extraordinary high transparency level (Fig. S2b). Furthermore, microprobe analyses (Fig. 2f) confirm the Ce^{3+} and Gd^{3+} amounts found by absorption measurements and nominal Gd^{3+}/Y^{3+} and Ga^{3+}/Al^{3+} ratios leading to important variation in the TL curves (see following part of the paper) in perfect agreement with previous results [27]. As pointed out in Table S1, the amount of Cr in the crystals is too small to be detected by elemental microprobe analysis but is estimated in this work through absorption measurements.

3.2. *Photoluminescence*

The excitation spectrum of the GYAGG:Ce,Ce crystals (Fig. 3) measured at 530 nm shows three main bands at 337, 414 and 460 nm. The first two correspond well to the 4f-5d^2 and 4f-5d^1 transitions of Ce^{3+}, respectively and are shifted both to higher energies with respect to

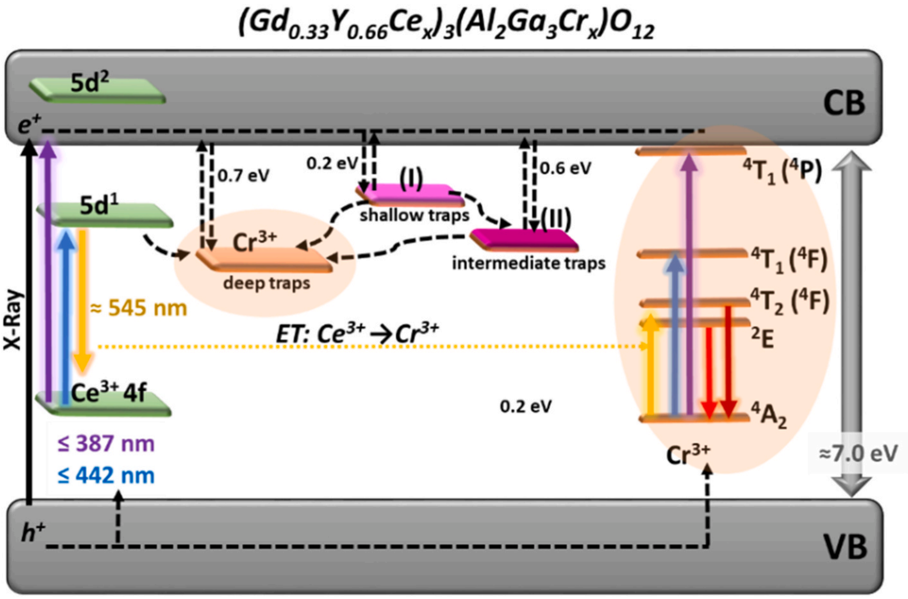

Fig. 4. Energy scheme of C5a ($(Gd_{0.33}Y_{0.66}Ce_x)_3(Al_2Ga_3Cr_x)O_{12}$). The values have been estimated based on the vacuum referred binding energy (VRBE) schemes of P. Dorenbos for $RE_3(Al_{1\text{-}x}Ga_x)_5O_{12}$ garnet compounds [26].

the previous absorption spectrum of Ce^{3+} (notice that in Ce:YAG containing no gadolinium and no gallium these bands are respectively at 344 and 436 nm). The peak at 460 nm corresponds to the $^4A_2$-$^4T_1$ (^4F) of Cr^{3+} as observed in powder samples of YAG:Cr^{3+} (see Ref. [34] and Fig. S4). Hence, an energy transfer takes place between Ce^{3+} and Cr^{3+}. Indeed, at 693 nm (Cr^{3+} emission), the relative intensity of the excitation bands changes and the peak at 460 nm becomes more intense. The additional narrow excitation band at 275 nm corresponds to the $^8S_{7/2}$-$^6I_{9/2}$ transition of Gd^{3+} observed in the absorption spectrum (Fig. S3a) and is well reported in the literature as the position of 4f-4f transitions do not change due to the shielding of the 4f orbitals. On the other hand, the emission spectrum shows the characteristic Ce^{3+} 5 d^1→4f transition at 532 nm and the Cr^{3+} ^2E→$^4A_2$ transition at 693 (N2) and 711 nm (N7) [34]. The same results are found for all crystals in Fig. S5. In addition, the emission spectra of C1.1b has been recorded at different UV-VIS excitation wavelengths and as expected there is no change in the wavelength position and the relative intensities are in agreement with the excitation spectrum (Fig. S6).

The emission spectra upon X-Ray excitation have been also recorded and the relative intensity of the Cr emission is significantly higher. Indeed the higher the Cr concentration within the crystals, the higher the relative intensity of Cr upon X-Ray in regards to Vis excitation (Fig. S7). In the case of X-Ray excitation, the much higher intensity of the Cr signal in the spectrum could be related with the generation of holes in the VB under X-Ray excitation and the ensuing Ce^{3+} to Ce^{4+} oxidation (see Fig. 4). It is important to mention that Cr^{2+} or [Cr^{3+}- e$^-$] species and Cr^{4+} or [Cr^{3+}-h$^+$] species generation may also take place from Cr^{3+}, although the concentration of the latter is much lower than that of Ce^{3+} [35,61] and are difficult to identify. It is also worth noticing that the different X-Rays excitation intensities have an impact on the mechanism as well. These results will be investigated hereafter by persistent luminescence and thermoluminescence measurements.

3.3. Thermoluminescence

Thermoluminescence (TL) is an essential tool to evaluate the persistent luminescence capabilities of the materials. In brief, the higher in temperature the afterglow peak (T_{max}), the deeper the traps and the longer the persistent luminescence will last. Nevertheless, there is an ideal range of temperatures for which the performance is optimum as too deep traps could not be thermally released and do not contribute to the persistent luminescence. In Fig. S8a, a typical TL experiment with C1.1a is shown. Upon LED Vis excitation at 10 K, a broad peak appears at around 288 K. This peak is the result of the integrated intensity of the persistent luminescence spectra either of the Ce^{3+} emission or of the Cr^{3+} emission. The fact that the position of the TL band (T_{max}) does not change indicates that there is an energy transfer process between Ce^{3+} and Cr^{3+} (Fig. 4). In addition, the Gd^{3+} and Ga^{3+} incorporation in the Y^{3+} and Al^{3+} sites, respectively, has an effect on the TL curve with respect to the YAG compound. A downwards and upwards shift of T_{max} is expected from literature upon incorporation of Gd^{3+} and Ga^{3+}, respectively [27]. In summary, T_{max} of C1.1-3 is located around 288 K, slightly lower than room temperature and lower than ideal temperature for applications [62]. Increasing yttrium content toward C5 sample favours the persistent luminescence (T_{max} of C5 is about 310–340 K) as presented in the following part of the paper.

The charging of the GYAGG: Ce, Cr crystals is effective with numerous energies corresponding to a wide range of wavelengths from the UV to the visible range. TL at selective wavelength irradiation at 10 K has been performed and reported for C1.1a crystal (see Fig. 5a). Notice that surprisingly in regard to other published compounds [11] T_{max} is almost constant whatever the excitation but the intensity strongly decreases under charging with smaller energies up to 650 nm. At 254 nm, 312 nm and 365 nm, the excitation is within the band gap and very efficient (Figs. 4 and 5) whereas at 450, 455, 470, 460 and 565 nm only Ce^{3+} is excited. Trap depth values can be obtained by the T_{max} position according to Urbach's formula ($E = T_{max}/500$) [63]. This is however, a rough estimation [64] as it makes no consideration of the curve shape. The same trap depth is always obtained for C1.1a at around 0.55 eV regardless of λ_{exc}, indicating that same traps related to Cr^{3+} are being filled. Notice that together with the main TL peak, a low temperature peak is observed around 80 K upon UV excitation. These shallower traps may correspond to the above-mentioned antisite defects or oxygen vacancies in YAGG [65] and are filled only when exciting into the Conduction Band (CB). Finally, at very low temperatures, luminescence is related to a thermal tunnelling effect, [66]. It is worth noticing here that these extremely shallow traps could also offer applications at very low temperature [1,67]. In Fig. S9 the persistent luminescence spectra of C1.1a has been compared at different points of the TL curve. Notice the higher intensity of Cr^{3+} emission upon UV excitation as observed in the photoluminescence experiments.

Secondly, TL experiments have been performed in the crystals with different amounts of Ce^{3+}, Cr^{3+} and Y^{3+}/Gd^{3+} ratio upon 455 nm LED excitation at 10 K (Fig. 5b). For C1.1-3 crystals, a main TL peak centred at around 288 K is present, with higher intensities and higher T_{max} upon higher amounts of Ce^{3+} (C1.2b) and Cr^{3+} (C1.1a, C1.1b), respectively These results are directly related with their afterglow curves shown hereafter at RT under the same excitation conditions with higher afterglow intensities for C1.1a, C1.1b and C1.2b (Fig. 6a). In terms of Y^{3+}/Gd^{3+} ratio, C5 exhibits traps corresponding well to the range 300–350 K for the glow curves as presented in Fig. 5b (trap depth 0.69 and 0.63 eV for C5a and C5b, respectively). This leads by a band gap modification to improved persistent luminescence in respect to C1.1-3 (Fig. 6a) due to the higher amount of Y^{3+}. In addition, the slightly higher amount of Ce^{3+} and Cr^{3+} in C5a with respect to C5b is beneficial (see Table S1). In fact, T_{max} of C5a (0.69 eV) is located within an optimum range of temperatures for enhanced persistent luminescence in comparison to other persistent luminescence materials such as $SrAl_2O_4$:Eu^{2+},Dy^{3+},B^{3+} and $Sr_4Al_{14}O_{25}$:Eu^{2+},Dy^{3+},B^{3+} (presented in Fig. S10 for the sake of comparison).

To move towards applications, these studies were enlarged to the TL glow curves of the various crystals upon sunlight excitation with a solar simulator at RT to simulate real charging conditions for outdoor applications (Fig. 5c, the excitation is performed at 300 K in the sun simulator and then the temperature is cooled down at 10 K before recording the TL glow curves.). Indeed, sunlight excitation is well-suited for garnets due to the large overlap of the sun emission and excitation spectrum of these GYAGG crystals [68]. In this case, two TL peaks appear at significantly higher T_{max} values (Inset Fig. 5c; $T_{max1} \approx 330$ K (0.66 eV), $T_{max2} \approx 365$ K (0.73 eV) for C1.1-3, $T_{max} \approx 340$ (0.68 eV) for C5b, and $T_{max} \approx 350$ K (0.70 eV) for C5a). The increase of T_{max} with the excitation temperature from 10 K to RT is due to the thermal depopulation of the traps under excitation at room temperature by about 0.064 eV (experimentally, in these crystals, T_{max} shifts about 0.0002 eV upwards for each difference of 1K in T_{exc}). The multicomponent profile is explained by the different λ_{exc} of sunlight.

TL glow curve profiles under sunlight excitation is difficult to analyze and present a structuration, probably related to the multi wavelengths of the sunlight emission profile, but with several traps at much higher T_{max} values, one can anticipate improved afterglow properties (Fig. S11a). On the other hand, we cannot rule out that optically stimulated emission (OSL) [69] may occur, which can even lead to traps redistribution [46, 70]. This OSL takes place upon long sunlight wavelengths excitation. Indeed, although the TL glow curve integrated intensities for the different GYAGG crystals, upon sunlight excitation at RT, follow the same trend as for blue excitation at 10 K (Fig. 5a), C1.1a with higher Cr^{3+} content exhibits a stronger improvement upon sunlight excitation in respect to blue excitation indicating possibly that OSL phenomenon occurs (Fig. S11b). Notice that the OSL could be even stronger in the crystals in regards to powdered samples thanks to the transparency and volume effect (see comparison of the relative TL intensities upon blue and sunlight excitation for C1.1b as pellet and as crystal in Fig. S11c).

Last, TL has been performed in C5a upon X-Ray excitation (Fig. S12a) in order to clarify if the same traps as under UV–Vis excitation are filled and shed light onto the mechanism. The energy shift of T_{max} after X-Ray excitation (318 K, 0.64 eV) in respect to the UV/Vis excitation (345 K, 0.69 eV) could be explained by the enhanced filling of the shallow and intermediate traps through the conduction band (Fig. 4), reflected in Fig. S12a as a TL peak at 110 K. Interestingly, and as already mentioned before, the luminescence spectra under X-Ray irradiation (Fig. S12b) shows a lower Ce/Cr ratio than under UV–Vis, probably due to the generation of holes in the VB under X-Ray excitation ensuring Ce^{3+} oxidation (see Fig. 4). This is actually the case between 10 and 250 K and above 430 K, where the TL of the sample does not play a role (Fig. S12b).

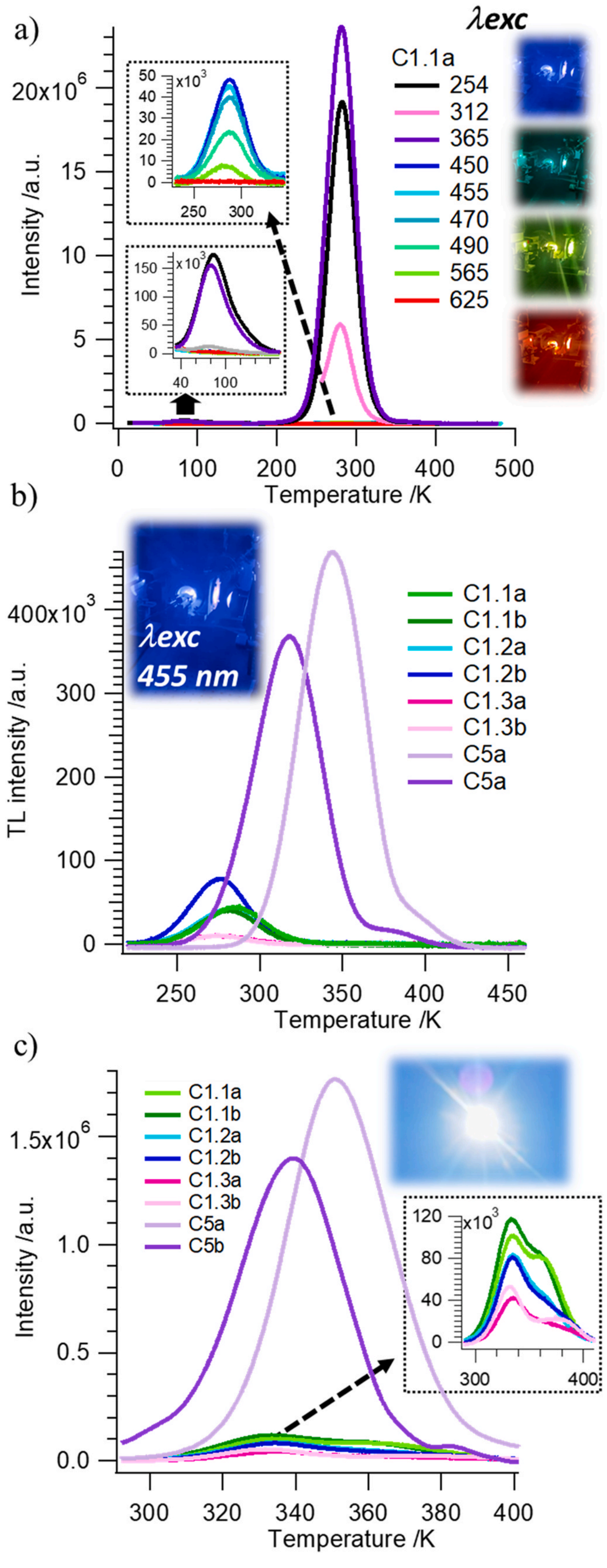

Fig. 5. Thermoluminescence curves a) of the crystal C1.1a after excitation at 10 K and different wavelengths, b) of all the GYAGG crystals after excitation at 10 K and 455 nm and c) of all GYAGG crystals after sunlight excitation at RT.

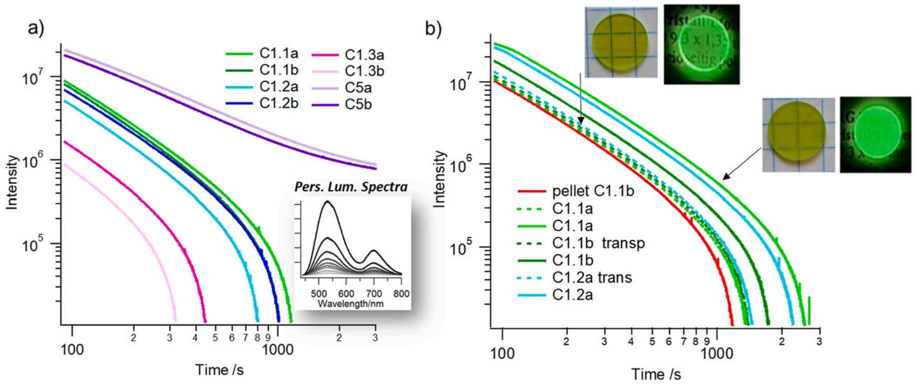

Fig. 6. Integrated Persistent luminescence intensity of $(Gd_xY_x)_3Ce_x(Al_2Ga_3Cr_x)O_{12}$ after excitation at 295 K with a 455 LED (1150 mW) during 10 min for the crystals a) with different composition (Inset: Persistent luminescence spectra) and b) with different volume and transparency.

3.4. *Persistent luminescence*

First, the persistent luminescence decay profiles recorded at two wavelengths corresponding to the Ce^{3+} emission at around 530 nm and Cr^{3+} emission at around 700 nm lead to the same shape for the two profiles (Fig. S8b), thanks to Ce/Cr energy transfers in agreement with the TL curve presented Fig. S8a. Secondly, tuning both the amount of dopants and the Y^{3+}/Gd^{3+} ratio, different afterglow curves have been obtained after excitation at 455 nm and at room temperature. These results are in line with the TL glow curves as presented above. Indeed, for the same Y^{3+}/Gd^{3+} and Ga^{3+}/Al^{3+} ratios, longer decays with higher initial afterglow are observed at higher amounts of Ce^{3+} and Cr^{3+} (Fig. 6a). More obvious though is the effect of Gd^{3+}. The latter favours the blue excitation but the performance is still better for higher amounts of Y^{3+} (Fig. 6a).

The second factor that has been modified is the volume and transparency of the crystals with less noticeable effects on their afterglow (example for C1.1-2 in Fig. 6b). First, Ce,Cr:GYAGG crystals show more intense afterglow than powders of exactly the same compositions (Fig. 6b red curve for a pellet of C1.1b and dark green curve for the crystal C1.1b). Second, thicker transparent crystals (1.5 mm thickness, dotted curves in Fig. 6b) exhibit as well more intense afterglow than thinner transparent crystals of 0.6 mm thickness (Fig. 6a) as a larger volume of the sample could be excited in the inner part of the material. This can be expressed as a volume effect [56,57]. Indeed, the initial intensities are 1.4, 1.7 and 2.9 times higher for the 1.5 mm crystals in regards to the 0.6 mm crystals for C1.1a, C1.1b and C1.2b, respectively.

Finally, the surfaces of the crystals have been polished with different qualities: two polishing were done during this work, (i) one laser quality with very good transparency (crystals described here before) within the faces and (ii) one de-polished quality where scattering occur towards the surface of the crystal (filled curves in Fig. 6b). This latter thus produces much more scattered light but favored the light extraction inducing a strong increase of the afterglow intensity and length. Persistent luminescence is indeed more intense than in the completely transparent samples due to the increased capability of light extraction related to the high refractive index difference between garnet crystals and air. Indeed, the initial intensities are 2.8, 1.6 and 2.0 times higher for the 1.5 mm de-polished crystals in regards to the 1.5 mm transparent crystals for C1.1a, C1.1b, and C1.2b, respectively (Fig. 6b). The same trends in transparency are observed for C5a.

3.5. *Quantum yield of fluorescence (QY_{fluor}) at RT and 455 nm excitation*

The quantum yield of fluorescence (QY_{fluor}) is obtained in an integrating sphere and the value is calculated as the ratio between the emission in the whole Ce^{3+} and Cr^{3+} ranges and the absorption, that is, the difference in the LED emission range without and with sample (see experimental details in the experimental section). The Ce^{3+}/Cr^{3+} emission ratio upon excitation at 405 nm is slightly higher than at 455 nm according to the excitation spectra. These emissions are exemplified in Fig. 7 for C5a. QY_{fluor} have been calculated for all crystals and QY_{fluor} ranges from 39% to 67% depending on the sample (Table S2). At first, we noticed that all crystals from the bottom (named b with smaller Cr content) present higher QY_{fluor} than the crystals from the top of the Czochralski boules (named a, containing higher Cr content), the enhancement is about 5% and this could be to related to the too high content of trivalent chromium co-doping in some part of the crystals that correspond to the observed Cr^{3+} emission (at about 700 nm) in the photoluminescence persistent luminescence spectra (Fig. 3). Furthermore, when comparing C1.1-3, the samples that present longer persistent luminescence exhibit the lower value of QY_{fluor} as indeed the trapping mechanism competes with the direct deactivation of Ce^{3+}. In other words, QY_{fluor} follows the trend: C1.3b > C1.1b > C1.3a>C1.2a≈C1.1a > C1.2b (Table S2 and Fig. S13), which is nearly the opposite to the trend of the integrated TL intensity: C1.2b > C1.2a > C1.1a > C1.1b > C1.3a > C1.3b. This is in agreement with our previous observations in $SrAl_2O_4{:}Eu^{2+},Dy^{3+}$ for which the best afterglow samples exhibit the shortest fluorescence lifetimes and lower QY_{fluor} due to a higher trap/activator ratio [71]. On the other hand, the higher amount of Y^{3+} in respect to Gd^{3+} in C5 leads to slightly higher QY_{fluo} (54%).

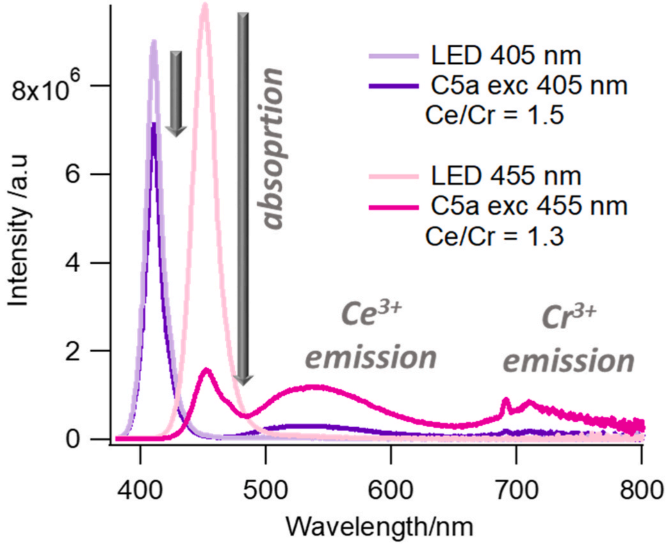

Fig. 7. Absorption and emission spectra of C5a upon 405 and 455 nm LED excitation, used to calculate QY_{fluor}.

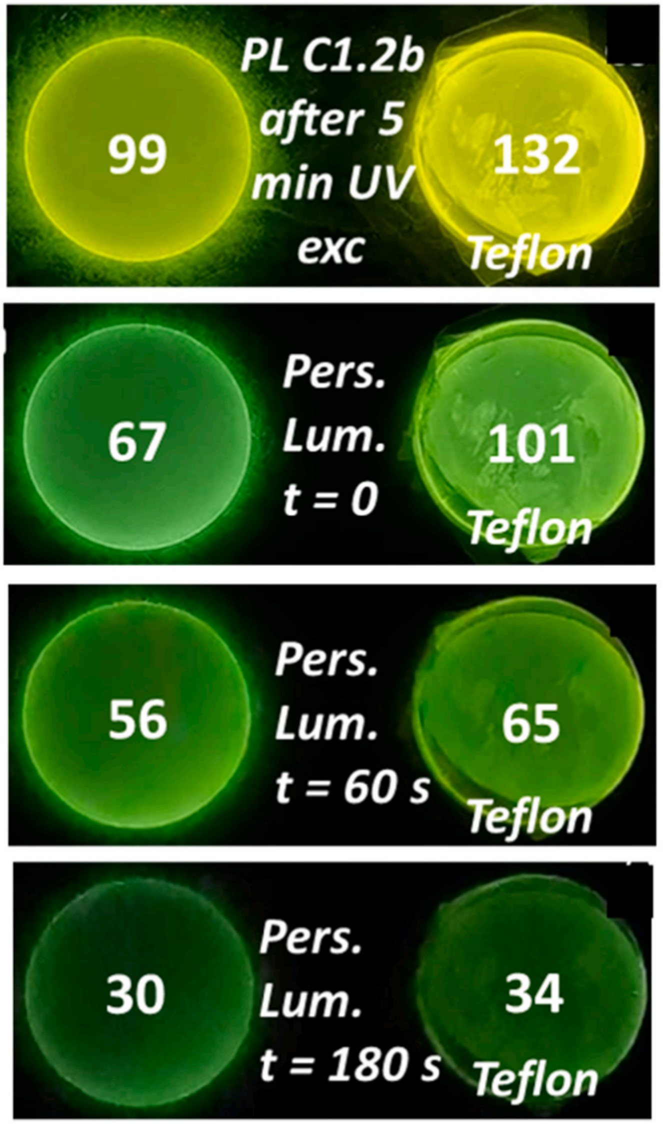

Fig. 8. Comparison of photoluminescence and Persistent luminescence of C1.2b with and without Teflon around the crystal. The numbers correspond to the relative PL and Persistent luminescence intensity measured with the ImageJ software within the same experimental set-up.

Finally, volume and transparency effects in QY_{fluor} and persistent luminescence intensities have been studied and the volume and surface treatment strongly control the persistent luminescence intensity for the same doping concentrations in the GYAGG crystals (Fig. 6b and Fig. S13). In the case of high polishing quality of the crystal surfaces, a large amount of the light is trapped inside the sample due to high value of the refractive index of the crystals in regard to the air (about 1.9 and 1 respectively) and the internal reflection law [72]. The extraction is favored as seen in Fig. 8 with unpolished surface, (smooth surface with 10 μm roughness) where the scattered light can be easily extracted as the extraction angles increased). Regarding the volume effect, when the values are normalized by the absorption, the persistent luminescence is enhanced in thicker samples. (Table S2).

3.6. *Optimizing light collection and tuning emission wavelengths*

The photoluminescence and persistent luminescence of the GYAGG crystals is maximum at the edges (Fig. 1) when the light extraction is more favourable. As observed in Fig. 8, the use of Teflon surrounding the crystals on the edges leads to an enhancement of the intensity of around 25% for the surface under UV excitation. Notice that the intensity was measured with the ImageJ software, and that the emission background has been subtracted. On the other hand, the persistent luminescence intensity for the sample with Teflon is 35% higher at time t = 0 and 15% and 10% higher after 1 min and 3 min of afterglow, respectively. Hence, covering the edges of the crystals where the emission was more concentrated enhances the emission in the surface. In other words, the crystal could act as a kind of persistent luminescence concentrator [72]. Notice that the intensity of the persistent luminescence is strongly dependent on the experimental condition and should be taken with care (see S14 the afterglow presented at room temperature after X-Ray excitation on a pellet and single crystal for sake of comparison). Finally, the wavelength of the persistent luminescence can be also tuned. It should be further noticed that increasing amounts of Y^{3+} favour a green emission whereas Gd^{3+} favours a yellow emission. This corresponds to a crystal field splitting variation in the wide garnet family [56].

4. Conclusions

Persistent luminescence Ce^{3+}, Cr^{3+}-doped GYAGG single crystals emitting in the green and red have been elaborated. The dopant and Y/Gd amounts have been varied, and the $[Gd_{0.33}Y_{0.67})_{3\text{-}x}Ce_x](Al_{2\text{-}y}Cr_y)Ga_3O_{12}$ crystal appears as the most interesting thanks to absorption, photoluminescence and thermoluminescence spectroscopies, in order to obtain the best persistent phosphor of the elaborated series while keeping the excitation with simple blue and sunlight very efficient. Cr^{3+} content strongly varies along the crystals while the Ce^{3+} content is quite small inside the crystals. Such single crystals can be very useful to study and better understand the persistent luminescence phenomena. For instance, within that single crystal the quantum yields can be measured and as expected for persistent luminescence compounds the quantum yield is far below 1, being between 0.39 and 0.67 for all samples. If the crystal composition is responsible of the main variation of the persistent luminescence intensity, with intensity increasing with cerium and chromium dopants, the main variation occurs when the yttrium content increases in regards to the gadolinium content. Furthermore, as expected volume effects have been shown to enhance the persistent luminescence intensity of the material whereas the surface polishing should be controlled with care to favour the light extraction within the crystals as the refractive indexes between the two media are quite important. Furthermore, as presented in the supplementary information section, we can further excite these materials by X-Rays in order to propose new applications such as anti-counterfeiting, therapy, X-Ray imaging, etc [73].

Declaration of competing interest

The authors declare that they have no known competing financial interests or personal relationships that could have appeared to influence the work reported in this paper.

Acknowledgements

This work was supported by the Swiss National Science Foundation (Postdoc. Mobility P400P2_191108/1) and the Agence Nationale de la Recherche (ANR-18-CE08-0012 PERSIST).

Appendix A. Supplementary data

Supplementary data to this article can be found online at https://doi.org/10.1016/j.ceramint.2023.02.249.

References

[1] D. Poelman, D. Van der Heggen, J. Du, E. Cosaert, P.F. Smet, Persistent phosphors for the future: fit for the right application, J. Appl. Phys. 128 (2020), 240903.

[2] A.S. Paterson, B. Raja, G. Garvey, A. Kolhatkar, A.E.V. Hagström, K. Kourentzi, T. R. Lee, R.C. Willson, Persistent luminescence strontium aluminate nanoparticles as reporters in lateral flow assays, Anal. Chem. 86 (2014) 9481–9488.

[3] L.-M. Pan, X. Zhao, X. Wei, L.-J. Chen, C. Wang, X.-P. Yan, Ratiometric luminescence aptasensor based on dual-emissive persistent luminescent nanoparticles for autofluorescence- and exogenous interference-free determination of trace aflatoxin B1 in food samples, Anal. Chem. 94 (2022) 6387–6393.

[4] P. Cruz, Super-LumiNova – the material that makes your watch glow (n.d.), https://www.montredo.com/super-luminova-the-material-that-makes-your-watch-glow/.

[5] Z. Rao, Y. Liao, Y. Zhu, X. Guo, M. Li, M. Ge, D. Gao, Study on alcoholysis recovery and performance of luminous materials in waste luminous fibers, Textil. Res. J. (2022), 00405175221088748.

[6] R. Barbosa, S.K. Gupta, B.B. Srivastava, A. Villarreal, H. De Leon, M. Peredo, S. Bose, K. Lozano, Bright and persistent green and red light-emitting fine fibers: a potential candidate for smart textiles, J. Lumin. 231 (2021), 117760.

[7] T. Kron, Applications of thermoluminescence dosimetry in medicine, Radiat. Protect. Dosim. 85 (1999) 333–340.

[8] N. Katumo, L.A. Ruiz-Preciado, V. Kumar, G. Hernandez-Sosa, B.S. Richards, I. A. Howard, Anticounterfeiting labels with smartphone-readable dynamic luminescent patterns based on tailored persistent lifetimes in Gd_2O_2S:Eu^{3+}/Ti^{4+}, Adv. Mater. Technol. 6 (2021), 2100047.

[9] N. Katumo, K. Li, B.S. Richards, I.A. Howard, Dual-color dynamic anti-counterfeiting labels with persistent emission after visible excitation allowing smartphone authentication, Sci. Rep. 12 (2022) 2100.

[10] T. Lécuyer, E. Teston, G. Ramirez-Garcia, T. Maldiney, B. Viana, J. Seguin, N. Mignet, D. Scherman, C. Richard, Chemically engineered persistent luminescence nanoprobes for bioimaging, Theranostics 6 (2016) 2488–2524.

[11] a) Bruno Viana, Cyrille Richard, Victor Castaing, Estelle Glais, Morgane Pellerin, Jianhua Liu, Corinne chanéac, NIR-persistent luminescence nanoparticles for bioimaging, principle and perspectives, in: A. Benayas, E. Hemmer, G. Hong, D. Jaque (Eds.), Infrared-Emit. Nanoparticles Biomed. Appl., Springer, Cham., 2020;
b) K. Sharma, A. Bessière, N. Basavaraju, K.R. Priolkar, L. Binet, B. Viana, D. Gourier, Interplay between chromium content and lattice disorder on persistent luminescence of $ZnGa_2O_4$: Cr^{3+} for in vivo imaging, J. Lumin. 155 (2015) 251–256.

[12] Z. Li, N. Yu, J. Zhou, Y. Li, Y. Zhang, L. Huang, K. Huang, Y. Zhao, S. Kelmar, J. Yang, G. Han, Coloring afterglow nanoparticles for high-contrast time-gating-free multiplex luminescence imaging, Adv. Mater. 32 (2020), 2003881.

[13] H. Chen, G.D. Wang, Y.-J. Chuang, Z. Zhen, X. Chen, P. Biddinger, Z. Hao, F. Liu, B. Shen, Z. Pan, J. Xie, Nanoscintillator-mediated X-ray inducible photodynamic therapy for in vivo cancer treatment, Nano Lett. 15 (2015) 2249–2256.

[14] J. Liu, T. Lécuyer, J. Seguin, N. Mignet, D. Scherman, B. Viana, C. Richard, Imaging and therapeutic applications of persistent luminescence nanomaterials, Adv. Drug Deliv. Rev. 138 (2019) 193–210.

[15] L.-X. Yan, L.-J. Chen, X. Zhao, X.-P. Yan, pH switchable nanoplatform for in vivo persistent luminescence imaging and precise photothermal therapy of bacterial infection, Adv. Funct. Mater. 30 (2020), 1909042.

[16] A. Bessière, J.-O. Durand, C. Noûs, Persistent luminescence materials for deep photodynamic therapy, Nanophotonics 10 (2021) 2999–3029.

[17] Afterglow Systems Near-the-Floor Safety System, (n.d.). https://www.swarco.com/products/road-markings/afterglow-systems/afterglow-systems.

[18] M. Li, H. Zhang, X. Zhang, J. Deng, Y. Liu, Z. Xia, B. Lei, Cr^{3+} doped $ZnGa_2O_4$ far-red emission phosphor-in-glass: toward high-power and color-stable plant growth LEDs with responds to all of phytochrome, Mater. Res. Bull. 108 (2018) 226–233.

[19] H. Sun, L. Pan, G. Zhu, X. Piao, L. Zhang, Z. Sun, Long afterglow $Sr_4Al_{14}O_{25}$:Eu,Dy phosphors as both scattering and down converting layer for CdS quantum dot-sensitized solar cells, Dalton Trans. 43 (2014) 14936–14941.

[20] H. Sun, L. Pan, X. Piao, Z. Sun, Enhanced performance of cadmium selenide quantum dot-sensitized solar cells by incorporating long afterglow europium, dysprosium co-doped strontium aluminate phosphors, J. Colloid Interface Sci. 416 (2014) 81–85.

[21] J. Zhang, J. Lin, J. Wu, S. Zhang, P. Zhou, X. Chen, R. Xu, Preparation of long persistent phosphor $SrAl_2O_4$:Eu^{2+}, Dy^{3+} and its application in dye-sensitized solar cells, J. Mater. Sci. Mater. Electron. 27 (2016) 1350–1356.

[22] Y. Li, M. Gecevicius, J. Qiu, Long persistent phosphors—from fundamentals to applications, Chem. Soc. Rev. 45 (2016) 2090–2136.

[23] a) J. Xu, S. Tanabe, Persistent luminescence instead of phosphorescence: history, mechanism, and perspective, J. Lumin. 205 (2019) 581–620;
b) A. Bessiere, A. Lecointre, R.A. Benhamou, E. Suard, G. Wallez, B. Viana, How to induce red persistent luminescence in biocompatible $Ca_3(PO_4)_2$, J. Mater. Chem. C 1 (6) (2013) 1252–1259.

[24] J. Ueda, Analysis of optoelectronic properties and development of new persistent phosphor in Ce^{3+}-doped garnet ceramics, J. Ceram. Soc. Jpn. 123 (2015) 1059–1064.

[25] J. Ueda, P. Dorenbos, A.J.J. Bos, K. Kuroishi, S. Tanabe, Control of electron transfer between Ce3+ and Cr^{3+} in the $Y_3Al_{5-x}Ga_xO_{12}$ host via conduction band engineering, J. Mater. Chem. C 3 (2015) 5642–5651.

[26] P. Dorenbos, Electronic structure and optical properties of the lanthanide activated $RE_3(Al_{1-x}Ga_x)_5O_{12}$ (RE=Gd, Y, Lu) garnet compounds, J. Lumin. 134 (2013) 310–318.

[27] K. Asami, J. Ueda, M. Kitaura, S. Tanabe, Investigation of luminescence quenching and persistent luminescence in Ce^{3+} doped (Gd,Y)$_3$(Al,Ga)$_5O_{12}$ garnet using vacuum referred binding energy diagram, J. Lumin. 198 (2018) 418–426.

[28] C.R. Stanek, K.J. McClellan, M.R. Levy, R.W. Grimes, Extrinsic defect structure of $RE_3Al_5O_{12}$ garnets, Phys. Status Solidi B 243 (2006) R75–R77.

[29] A.B. Muñoz-García, Z. Barandiarán, L. Seijo, Antisite defects in Ce-doped YAG ($Y_3Al_5O_{12}$): first-principles study on structures and 4f–5d transitions, J. Mater. Chem. 22 (2012) 19888–19897.

[30] a) C.R. Stanek, K.J. McClellan, M.R. Levy, C. Milanese, R.W. Grimes, The effect of intrinsic defects on $RE_3Al_5O_{12}$ garnet scintillator performance, Proc. 11th Symp. Radiat. Meas. Appl. 579 (2007) 27–30;
b) M. Fasoli, A. Vedda, M. Nikl, C. Jiang, B.P. Uberuaga, D.A. Andersson, K. J. McClellan, C.R. Stanek, Band-gap engineering for removing shallow traps in rare-earth Lu3Al5O12 garnet scintillators using Ga3+ doping, Phys. Rev. B 84 (2011), 081102(R).

[31] Y.-C. Lin, M. Bettinelli, M. Karlsson, Unraveling the mechanisms of thermal quenching of luminescence in Ce^{3+}-doped garnet phosphors, Chem. Mater. 31 (2019) 3851–3862.

[32] H. Nakamura, K. Shinozaki, T. Okumura, K. Nomura, T. Akai, Massive red shift of Ce^{3+} in $Y_3Al_5O_{12}$ incorporating super-high content of Ce, RSC Adv. 10 (2020) 12535–12546.

[33] Y.-C. Lin, P. Erhart, M. Bettinelli, N.C. George, S.F. Parker, M. Karlsson, Understanding the interactions between vibrational modes and excited state relaxation in $Y_{3-x}Ce_xAl_5O_{12}$: design principles for phosphors based on 5d–4f transitions, Chem. Mater. 30 (2018) 1865–1877.

[34] Y. Katayama, B. Viana, D. Gourier, J. Xu, S. Tanabe, Photostimulation induced persistent luminescence in $Y_3Al_2Ga_3O_{12}$:Cr^{3+}, Opt. Mater. Express 6 (2016) 1405–1413.

[35] J. Xu, J. Ueda, Y. Zhuang, B. Viana, S. Tanabe, $Y_3Al_{5-x}Ga_xO_{12}$:Cr^{3+}: a novel red persistent phosphor with high brightness, APEX 8 (2015), 042602.

[36] J. Ueda, A. Hashimoto, S. Takemura, K. Ogasawara, P. Dorenbos, S. Tanabe, Vacuum referred binding energy of 3d transition metal ions for persistent and photostimulated luminescence phosphors of cerium-doped garnets, J. Lumin. 192 (2017) 371–375.

[37] W.S. Silveira, A.J.S. Silva, P.A.M. do Nascimento, I. da S. Carvalho, M.V. dos S. Rezende, Improving the luminescence properties of YAG:Ce^{3+} phosphors by co-doping Sr^{2+} ions, J. Lumin. 231 (2021), 166363.

[38] W. Li, Y. Zhuang, P. Zheng, T.-L. Zhou, J. Xu, J. Ueda, S. Tanabe, L. Wang, R.-J. Xie, Tailoring trap depth and emission wavelength in $Y_3Al_{5-x}Ga_xO_{12}$:Ce^{3+},V^{3+} phosphor-in-glass films for optical information storage, ACS Appl. Mater. Interfaces 10 (2018) 27150–27159.

[39] J. Ueda, S. Miyano, S. Tanabe, Formation of deep electron traps by Yb3+ codoping leads to super-long persistent luminescence in Ce^{3+}-doped yttrium aluminum gallium garnet phosphors, ACS Appl. Mater. Interfaces 10 (2018) 20652–20660.

[40] D. Zhou, Z. Wang, Z. Song, F. Wang, S. Zhang, Q. Liu, Enhanced persistence properties through modifying the trap depth and density in $Y_3Al_2Ga_3O_{12}$:Ce^{3+},Yb^{3+} phosphor by Co-doping B3+, Inorg. Chem. 58 (2019) 1684–1689.

[41] J. Bierwagen, T. Delgado, G. Jiranek, S. Yoon, N. Gartmann, B. Walfort, M. Pollnau, H. Hagemann, Probing traps in the persistent phosphor $SrAl_2O_4$:Eu^{2+},Dy^{3+},B^{3+} - a wavelength, temperature and sample dependent thermoluminescence investigation, J. Lumin. (2020), 117113.

[42] S. Yoon, J. Bierwagen, M. Trottmann, B. Walfort, N. Gartmann, A. Weidenkaff, H. Hagemann, S. Pokrant, The influence of boric acid on improved persistent luminescence and thermal oxidation resistance of $SrAl_2O_4$:Eu^{2+}, J. Lumin. 167 (2015) 126–131.

[43] T. Delgado, S. Ajoubipour, J. Afshani, S. Yoon, B. Walfort, H. Hagemann, Spectroscopic properties of Dy^{3+}- and Dy^{3+}, B^{3+}- doped $SrAl_2O_4$, Opt. Mater. 89 (2019) 268–275.

[44] P. Dorenbos, f d transition energies of divalent lanthanides in inorganic compounds, J. Phys. Condens. Matter 15 (2003) 575–594.

[45] J. Xu, J. Ueda, S. Tanabe, Novel persistent phosphors of lanthanide–chromium co-doped yttrium aluminum gallium garnet: design concept with vacuum referred binding energy diagram, J. Mater. Chem. C 4 (2016) 4380–4386.

[46] J. Xu, D. Murata, J. Ueda, B. Viana, S. Tanabe, Toward rechargeable persistent luminescence for the first and third biological windows via persistent energy transfer and electron trap redistribution, Inorg. Chem. 57 (2018) 5194–5203.

[47] J. Xu, S. Tanabe, A.D. Sontakke, J. Ueda, Near-infrared multi-wavelengths long persistent luminescence of Nd3+ ion through persistent energy transfer in Ce^{3+}, Cr^{3+} co-doped Y3Al2Ga3O12 for the first and second bio-imaging windows, Appl, Phys. Lett. 107 (2015), 081903.

[48] J. Xu, D. Murata, J. Ueda, S. Tanabe, Near-infrared long persistent luminescence of Er^{3+} in garnet for the third bio-imaging window, J. Mater. Chem. C 4 (2016) 11096–11103.

[49] Laura A. Sordillo, Pu Yang, Sebastião Pratavieira, Yury Budansky, Robert R. Alfano, Deep optical imaging of tissue using the second and third near-infrared spectral windows, J. Biomed. Opt. 19 (2014), 056004.

[50] Z. Feng, T. Tang, T. Wu, X. Yu, Y. Zhang, M. Wang, J. Zheng, Y. Ying, S. Chen, J. Zhou, X. Fan, D. Zhang, S. Li, M. Zhang, J. Qian, Perfecting and extending the near-infrared imaging window, Light Sci. Appl. 10 (2021) 197.

[51] L. Wu, J. Hu, Q. Zou, Y. Lin, D. Huang, D. Chen, H. Lu, H. Zhu, Synthesis and optical properties of a $Y_3(Al/Ga)_5O_{12}$:Ce^{3+},Cr^{3+},Nd^{3+} persistent luminescence nanophosphor: a promising near-infrared-II nanoprobe for biological applications, Nanoscale 12 (2020) 14180–14187.

[52] E. Arroyo, B. Torres Herrero, J.M. de la Fuente, M. Ocaña, A.I. Becerro, Highly uniform $Y_3Al_2Ga_3O_{12}$-based nanophosphors for persistent luminescence bioimaging in the visible and NIR regions, Inorg. Chem. Front. 9 (2022) 2454–2461.

[53] V. Boiko, Z. Dai, M. Markowska, C. Leonelli, C. Mortalò, F. Armetta, F. Ursi, G. Nasillo, M.L. Saladino, D. Hreniak, Particle size-related limitations of persistent phosphors based on the doped $Y_{(3)}Al_{(2)}Ga_{(3)}O_{(12)}$ system, Sci. Rep. 11 (2021), 141–141.

[54] P. Sengar, D.-L. Flores, K. Chauhan, B. Can-Uc, K. Juarez-Moreno, O.E. Contreras, M.A. Digman, G.A. Hirata, Visible/Near-Infrared emitting, garnet-based paramagnetic-persistent luminescent nanocrystals for two-photon bioimaging, Cryst. Growth Des. 20 (2020) 5880–5889.

[55] X. Wang, Y. Chen, P.A. Kner, Z. Pan, Gd3+-activated narrowband ultraviolet-B persistent luminescence through persistent energy transfer, Dalton Trans. 50 (2021) 3499–3505.

[56] J. Ueda, K. Kuroishi, S. Tanabe, Yellow persistent luminescence in Ce^{3+}–Cr^{3+}-codoped gadolinium aluminum gallium garnet transparent ceramics after blue-light excitation, APEX 7 (2014), 062201.

[57] J. Xu, J. Ueda, K. Kuroishi, S. Tanabe, Fabrication of Ce3+–Cr3+ co-doped yttrium aluminium gallium garnet transparent ceramic phosphors with super long persistent luminescence, Scripta Mater. 102 (2015) 47–50.

[58] V. Castaing, G. Lozano, H. Míguez, Transparent phosphor thin films based on rare-earth-doped garnets: building blocks for versatile persistent luminescence materials, Adv. Photonics Res. n/a (2022), 2100367.

[59] T. Delgado, J. Afshani, H. Hagemann, Spectroscopic study of a single crystal of $SrAl_2O_4$:Eu^{2+}:Dy^{3+}, J. Phys. Chem. C 123 (2019) 8607–8613.

[60] N. Basavaraju, S. Sharma, A. Bessière, B. Viana, D. Gourier, K.R. Priolkar, Red persistent luminescence in $MgGa_2O_4$: Cr^{3+}; a new phosphor for in vivo imaging, J. Phys. Appl. Phys. 46 (2013), 375401.

[61] V. Boiko, J. Zeler, M. Markowska, Z. Dai, A. Gerus, P. Bolek, E. Zych, D. Hreniak, Persistent luminescence from $Y_3Al_2Ga_3O_{12}$ doped with Ce^{3+} and Cr^{3+} after X-ray and blue light irradiation, J. Rare Earths 37 (2019) 1200–1205.

[62] J. Du, O.Q. De Clercq, D. Poelman, Temperature dependent persistent luminescence: evaluating the optimum working temperature, Sci. Rep. 9 (2019), 10517.

[63] F. Urbach, Zur lumineszenz der alkalihalogenide, Sitzungsberichte Akad Wiss Wien 139 (1930) 363–372.

[64] N. Chandrasekhar, K.B. Singh, R.K. Gartia, On the Urbach's formula for evaluation of electron trapping parameter: the case of persistent luminescent materials, J. Rare Earths 35 (2017) 733–738.

[65] T. Yang, H. Jiang, O. Hai, Y. Dong, S. Liu, S. Gao, Effect of oxygen vacancies on the persistent luminescence of $Y_3Al_2Ga_3O_{12}$:Ce^{3+},Yb^{3+} phosphors, Inorg. Chem. 60 (2021) 17797–17809.

[66] V. Liepina, D. Millers, K. Smits, Tunneling luminescence in long lasting afterglow of $SrAl_2O_4$:Eu,Dy, J. Lumin. 185 (2017) 151–154.

[67] V. Vitola, V. Lahti, I. Bite, A. Spustaka, D. Millers, M. Lastusaari, L. Petit, K. Smits, Low temperature afterglow from $SrAl_2O_4$: Eu, Dy, B containing glass, Scripta Mater. 190 (2021) 86–90.

[68] J. Botterman, P.F. Smet, Persistent phosphor $SrAl_2O_4$:Eu,Dy in outdoor conditions: saved by the trap distribution, Opt Express 23 (2015) A868–A881.

[69] D. Van der Heggen, J.J. Joos, P.F. Smet, Importance of evaluating the intensity dependency of the quantum efficiency: impact on LEDs and persistent phosphors, ACS Photonics 5 (2018) 4529–4537.

[70] D. Van der Heggen, J.J. Joos, A. Feng, V. Fritz, T. Delgado, N. Gartmann, B. Walfort, D. Rytz, H. Hagemann, D. Poelman, B. Viana, P.F. Smet, Persistent Luminescence in Strontium Aluminate: a Roadmap to a Brighter Future, n/a, 2022, 2208809.

[71] T. Delgado, N. Gartmann, B. Walfort, F. LaMattina, M. Pollnau, A. Rosspeintner, J. Afshani, J. Olchowka, H. Hagemann, Fundamental Loading-Curve Characteristics of the Persistent Phosphor $SrAl_2O_4$:Eu^{2+},Dy^{3+},B^{3+}: the Effect of Temperature and Excitation Density, Adv. Photonics Res. n/a, 2022, 2100179.

[72] T. Gallinelli, A. Barbet, F. Druon, F. Balembois, P. Georges, T. Billeton, S. Chenais, S. Forget, Enhancing brightness of Lambertian light sources with luminescent concentrators: the light extraction issue, Opt Express 27 (Issue 8) (2019) 11830–11843.

[73] C. Richard, B. Viana, Persistent X-ray-activated phosphors: mechanisms and applications, Light Sci. Appl. 11 (2022) 1–3.